NANO · MICRO small
www.small-journal.com

In Vivo Near-Infrared Imaging Using Ternary Selenide Semiconductor Nanoparticles with an Uncommon Crystal Structure

Jingke Yao, José Lifante, Paloma Rodríguez-Sevilla, María de la Fuente-Fernández, Francisco Sanz-Rodríguez, Dirk H. Ortgies, Oscar Gomez Calderon, Sonia Melle, Erving Ximendes, Daniel Jaque, and Riccardo Marin**

The implementation of in vivo fluorescence imaging as a reliable diagnostic imaging modality at the clinical level is still far from reality. Plenty of work remains ahead to provide medical practitioners with solid proof of the potential advantages of this imaging technique. To do so, one of the key objectives is to better the optical performance of dedicated contrast agents, thus improving the resolution and penetration depth achievable. This direction is followed here and the use of a novel $AgInSe_2$ nanoparticle-based contrast agent (nanocapsule) is reported for fluorescence imaging. The use of an Ag_2Se seeds-mediated synthesis method allows stabilizing an uncommon orthorhombic crystal structure, which endows the material with emission in the second biological window (1000–1400 nm), where deeper penetration in tissues is achieved. The nanocapsules, obtained via phospholipid-assisted encapsulation of the $AgInSe_2$ nanoparticles, comply with the mandatory requisites for an imaging contrast agent—colloidal stability and negligible toxicity—and show superior brightness compared with widely used Ag_2S nanoparticles. Imaging experiments point to the great potential of the novel $AgInSe_2$-based nanocapsules for high-resolution, whole-body in vivo imaging. Their extended permanence time within blood vessels make them especially suitable for prolonged imaging of the cardiovascular system.

1. Introduction

Among other conditions, the prosperity of our society depends on a sustainable health system. To that end, access to diagnostic approaches that are fast, inexpensive, and that minimize the discomfort of the patient is pivotal. Currently available techniques, such as magnetic resonance imaging, X-ray computed tomography, and nuclear imaging, offer ever improving performance, but in turn require sophisticated equipment and elevated maintenance costs. In recent years, fluorescence imaging (FI) has been emerging as a credible complementary technique to those mentioned above.[1] The advantages of FI reside in the use of nonionizing radiation, simple and less expensive setups, minimal invasiveness, and real-time image-acquisition capabilities. However, its main limitation is the difficulty in obtaining deep-tissue and high-resolution in vivo images owing to the large attenuation of

J. Yao, J. Lifante, P. Rodríguez-Sevilla, F. Sanz-Rodríguez, D. H. Ortgies, E. Ximendes, D. Jaque, R. Marin
Nanomaterials for Bioimaging Group (NanoBIG)
Facultad de Ciencias
Universidad Autónoma de Madrid
C/Francisco Tomás y Valiente 7, Madrid 28049, Spain
E-mail: daniel.jaque@uam.es; riccardo.marin@uam.es

J. Lifante, P. Rodríguez-Sevilla, F. Sanz-Rodríguez, D. H. Ortgies, E. Ximendes, D. Jaque
Nanomaterials for Bioimaging Group (NanoBIG)
Instituto Ramón y Cajal de Investigación Sanitaria
Hospital Ramón y Cajal
Ctra. De Colmenar Viejo, Km. 9100, Madrid 28034, Spain

The ORCID identification number(s) for the author(s) of this article can be found under https://doi.org/10.1002/smll.202103505.

© 2021 The Authors. Small published by Wiley-VCH GmbH. This is an open access article under the terms of the Creative Commons Attribution License, which permits use, distribution and reproduction in any medium, provided the original work is properly cited.

DOI: 10.1002/smll.202103505

J. Lifante, M. de la Fuente-Fernández
Nanomaterials for Bioimaging Group (NanoBIG)
Departamento de Fisiología
Facultad de Medicina
Universidad Autónoma de Madrid
Avda. Arzobispo Morcillio 2, Madrid 28029, Spain

F. Sanz-Rodríguez
Nanomaterials for Bioimaging Group (NanoBIG)
Departmento de Biología, Facultad de Ciencias
Universidad Autónoma de Madrid
C/Darwin, 2, Madrid 28049, Spain

O. G. Calderon, S. Melle
Department of Optics
Complutense University of Madrid
Madrid 28037, Spain

light into tissues.[2,3] The future application of FI at the clinical level as a viable alternative to conventional imaging techniques for selected applications passes through the development of more efficient detection systems as well as novel contrast agents. In this vein, luminescent nanoparticles (NPs) hold great promise.

In search for the most suitable NP-based contrast agents, it soon became clear that in vivo images of the highest quality could be obtained with NPs emitting in the so-called biological transparency windows.[4–7] These are near-infrared (NIR) spectral ranges where biological tissues are less impervious to the electromagnetic radiation, with NIR-I and NIR-II spanning over the 750–950 nm and 1000–1400 nm ranges, respectively.[8] The latest generation of luminescent NPs employed in FI emit in the NIR-II, wherein the low scattering coefficient and reduced absorption from tissue components result in significantly improved penetration depth and resolution of the fluorescence images.[5] The use of NPs emitting in the NIR-II has made enabled, for example, the acquisition of high-resolution in vivo images of the cardiovascular system, anatomical images of animal models, as well as molecular imaging of infarcted heart.[9–15] Carbon nanotubes, lanthanide-doped NPs, and semiconductor NPs are the most representative FI contrast agents.[16] In fact, many of the most significant advances in NIR-II FI have been obtained with semiconductor NPs made of Ag_2S.[14,17–23]

Ag_2S NPs possess good biocompatibility and physicochemical stability,[24] but their performance is severely limited by their low brightness, which stems from low photoluminescence quantum yield (PLQY; ≈ 0.1% for commercially available Ag_2S) and limited molar absorption coefficient (4×10^{-5} M^{-1} cm^{-1} at 800 nm, an optimal excitation wavelength for in vivo FI).[25–27] Moreover, methods to increase their optical performance are scarce, sometimes requiring special equipment and often affording limited improvement.[25,28,29] Therefore, the development of NIR-II-emitting semiconductor NPs that are brighter is an urgent matter. $AgInS_2$ and $AgInSe_2$ (AISe) NPs, for instance, offer a plausible alternative to Ag_2S NPs, owing to their higher (>20%) PLQY and their good photostability.[30,31] Their ternary nature also allows to finely manipulate their composition via selective cation exchange.[32] However, to the best of our knowledge, AISe NPs have been investigated only once as in vivo FI contrast agents by Deng et al., who performed tumor imaging using arginylglycylaspartic acid (RGD)-decorated AISe/ZnS core/shell NPs.[33] In that study, AISe NPs show an emission centered at 800 nm, imposing the use of an excitation wavelength lying outside of the biological windows (660 nm). Thus, the authors obtained in vivo fluorescence images of limited resolution. Being able to push the operating range of AISe NPs into NIR-I and NIR-II—in terms of excitation and emission, respectively—would allow achieving images of much higher quality.

To address this issue, in this work we take advantage of a synthesis method that provides AISe NPs with an uncommon crystal structure, which in turn leads to an NIR-II-centered emission. The hydrophobic NPs are transferred to aqueous media by encapsulating them in a phospholipid layer. The so-obtained colloidally stable nanocapsules (NCs) are tested for their toxicity in vitro and later utilized as contrast agents for in vivo FI. Comparison of the results obtained with AISe NCs and commercial Ag_2S NPs underscores the excellent performance of the newly developed contrast agents particularly for the visualization of the vasculature, opening the door to further studies on the use of this material for FI.

2. Results and Discussion

The synthesized AISe NPs showed a triangular shape in transmission electron microscopy (TEM) images—which suggested a tetrahedral habit—and an average size of (8 ± 2) nm (**Figure 1**A and Figure S1, Supporting Information). They could be easily dispersed in nonpolar organic solvents such as tetrachloroethylene (TCE), yielding an optically clear dispersion (Figure 1B). The diffraction pattern of AISe NPs featured broad reflections characteristic of nanometric crystalline domains (Figure 1C). Both the morphology and the diffraction pattern were consistent with the data reported by Langevin et al.[34] Moreover, elemental mapping showed the simultaneous presence of Ag, In and Se, further corroborating the nature of the produced material (Figure S2, Supporting Information). It is worth noting that these AISe NPs possess an unusual orthorhombic crystalline phase that was first reported by Vittal and co-workers,[35] rather than the more common tetragonal polymorph.[36,37] The reason for this has to be searched in the NP formation mechanism, which entails orthorhombic Ag_2Se seeds as an intermediate. The subsequent cation exchange with In^{3+} yields $AgInSe_2$ that are isostructural to orthorhombic $AgInS_2$ (*Pna2₁* space group).[34] Therefore, the crystal structure of AISe NPs has memory of the structure of parent Ag_2Se seeds. This uncommon crystal structure is likely the responsible for the unique optical properties of these NPs (vide infra). Upon transfer to aqueous media with the aid of phospholipids (Figure 1D), the $AgInSe_2$ NPs arranged in quasi-spherical aggregates (Figure 1A, right). These nanocapsules form due to two competitive hydrophobic interactions: i) between 1-dodecanethiol (DDT) molecules attached to the surface of the NPs and the hydrophobic tail of the phospholipids and ii) between DDT molecules on the surface of different NPs. The stability of the AISe NCs in aqueous media was confirmed by dynamic light scattering (DLS) measurements, which showed a sizeable increase of the effective diameter when passing from TCE to phosphate buffer saline (PBS) 1x (Figure 1E, left). We further tested the colloidal stability of the AISe NCs in PBS over the 15–55 °C temperature range (Figure 1E, middle), observing negligible changes in the hydrodynamic diameter (≈150 nm; Z-average) and in the polydispersion index (≈0.2). As expected, the measured Z-potential was negative (−33 mV), due to the partial hydrolyzation of the maleimide groups on the surface of AISe NCs (Figure 1E, right).[38] This hydrolyzation ultimately resulted in the appearance of carboxylic groups, whose deprotonation in aqueous media leads to an overall negative surface charge. The use of phospholipids with maleimide was preferred due to the documented increased interaction of NPs featuring this functional group toward cellular thiols.[39] To further confirm the presence of phospholipids on the surface of the NCs, Fourier-transform infrared (FTIR) spectra of the as-synthesized AISe NPs and AISe NCs were collected and compared with the spectra of pristine organic molecules (Figure 1F). Upon encapsulation of the AISe NPs in phospholipids, the signals originating from 1,2-distearoylsn-glycero-3-phosphoethanolamine-*N*-[maleimide(polyethylene

© 2021 The Authors. Small published by Wiley-VCH GmbH

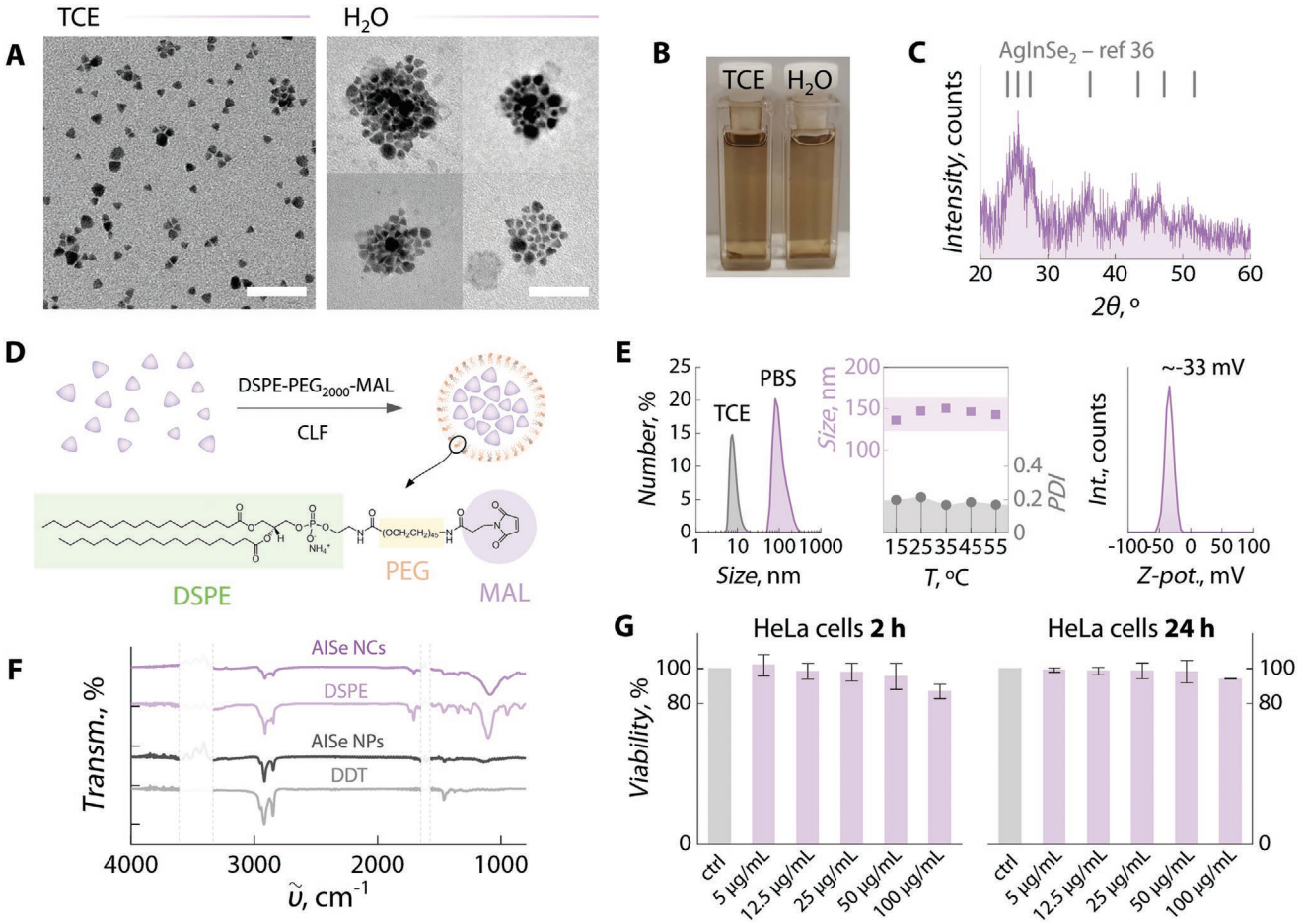

Figure 1. Characterization of the morphology, structure, surface chemistry, and cytotoxicity of AISe NPs and NCs. A) TEM images before and after phospholipid-assisted transfer to water. Scale bars are 50 nm. B) Optical image of a dispersion of AISe NPs in TCE and AISe NCs in water. C) PXRD pattern of AISe NPs, along with the position of the main reflections reported in ref. [14] for the same material. D) Scheme of the encapsulation mechanism, along with the chemical structure of the DSPE-PEG_{2000}-MAL phospholipids used for preparing AISe NCs. E) DLS and Z-potential measurements performed on AISe NPs (in TCE) and AISe NCs (DLS in PBS 1x and Z-potential in water). The values reported for the hydrodynamic diameter of AISe NCs versus temperature are Z-average values given by the software. F) FTIR spectra of AISe NPs and AISe NCs, along with the spectra of pristine DDT and DSPE-PEG_{2000}-MAL. The areas shaded in white correspond to ranges where spurious signals originating during the background subtraction procedure are located. G) Cell viability tests performed on HeLa cells after 2 and 24 h of cell incubation with a AISe NCs concentration between 5 and 100 μg mL^{-1}.

glycol)-2000] (ammonium salt) Maleimide (DSPE-PEG_{2000}-MAL) became dominant over those coming from DDT, thus confirming the presence of amphiphilic molecules in the NCs. We then tested the cytotoxicity of AISe NCs, incubating HeLa cells at different concentrations (5–100 μg mL^{-1}) for 2 and 24 h (Figure 1G). The results did not indicate appreciable toxicity, with a maximum cell viability decrease of 13% after 2 h of incubation at an AISe NCs concentration of 100 μg mL^{-1}. The absence of cell toxicity of our NCs is in agreement with previous works reporting good biocompatibility of $AgInSe_2$ NPs against cancerous and normal cell lines.[40] Altogether, the observed excellent colloidal stability in PBS along with the lack of substantial toxicity indicated the amenability of the developed NCs to applications in the biomedical context.

Subsequently, the optical properties of the material were assessed. As can be observed in **Figure 2**A, while the extinction spectrum is not affected by the dispersing solvent, AISe NCs in water exhibited an emission that is slightly blueshifted and narrower compared to the one of parents AISe NPs dispersed in TCE. This change in the emission spectral profile is the result of the inner filter effect exerted by water, which has strong absorption bands in the wavelength range investigated (Figure S3A, Supporting Information).[41] As expected, the transfer to water induced a sizeable (83%) intensity decrease (Figure S3B, Supporting Information), which was attributed to the activation of nonradiative de-excitation events involving water vibrations.[42] To benchmark the brightness of AISe NCs, we compared their optical properties with those of commercial Ag_2S NPs (Figure 2B–D). NIR images acquired under 800 nm excitation with the in vivo optical setup (see the Experimental Section) show that AISe NCs have a much brighter luminescence compared with Ag_2S NPs (Figure 2B,C). In fact, the measured absolute PLQY of AISe NCs was (3.9 ± 0.1)% (Figure S4, Supporting Information). The molar extinction coefficient (ε) of these particles was calculated to be roughly 3.5 times smaller at 800 nm than the one Ag_2S NPs (Figure 2D; see also the Supporting

© 2021 The Authors. Small published by Wiley-VCH GmbH

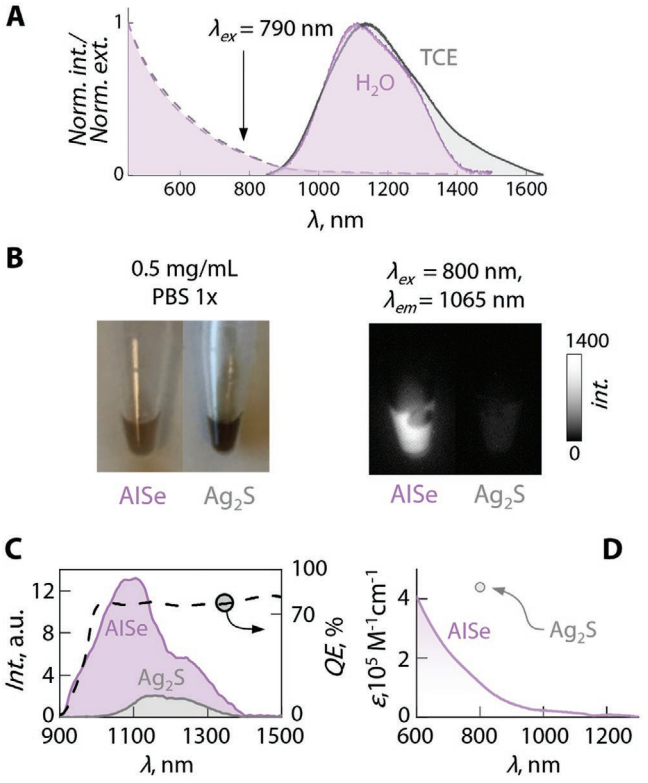

Figure 2. A) Absorption (dashed lines) and emission (solid lines, λ_{ex} = 790 nm) spectra of AISe NPs in TCE (gray) and AISe NCs in water (purple). B) Optical (left) and NIR-II (right) image of two centrifuge tubes containing a dispersion of AISe NCs and Ag_2S NPs (0.5 mg mL^{-1}). C) Comparison of the emission spectra obtained at the in vivo imaging setup. The response curve (quantum efficiency, QE) of the detector is also reported (dashed gray line). D) Calculated molar extinction coefficient of an AISe NCs dispersion in water (purple line) and the value for commercial Ag_2S NPs at 800 nm (gray dot) obtained from ref. [25].

Information for details about these calculations). Therefore, since the brightness is defined as the product between ε and PLQY, according to the above observations our AISe NCs boast a brightness of 4.5×10^3 M^{-1} cm^{-1}, roughly one order of magnitude larger than the one determined for commercial Ag_2S NPs in ref. [25] (i.e., 5.9×10^2 M^{-1} cm^{-1}). Admittedly, optimization of the reaction conditions[28] or use of ultrafast photochemistry methods[25] allows producing Ag_2S NPs brighter than their commercial counterpart. However, we should point out that our synthesis protocol did not undergo any optimization. It is thus expected that further adjustment of the synthesis conditions and, possibly, exploitation of selective cation exchange[32] could push the brightness of AISe NCs to even higher values. Nonetheless, the brightness of the herein presented NCs is high enough to allow deep tissue images to be recorded. Indeed, the luminescence of a 1 mg mL^{-1} dispersion in PBS 1x could be recorded through several millimeters of chicken breast tissue under 800 nm excitation using a power density of 50 mW cm^{-2} (Figure S5, Supporting Information).

To complete the characterization of our AISe NCs, we also investigated the temperature dependence of their photoluminescence. As shown in detail in Figure S6 in the Supporting Information, the thermal sensitivities retrieved for intensity- and lifetime-based thermometric approaches were 4.5 and 3% $°C^{-1}$ respectively at 37 °C. These numbers are similar to those reported previously for Ag_2S NP-based luminescent thermometers used for in vivo thermal sensing.[18,20,43] Moreover, as demonstrated above, AISe NCs are brighter and should therefore provide higher spatiotemporal resolutions. Thus, although the use of AISe NCs as thermal sensors lies outside the scope of this study, these nanoprobes hold great potential as biocompatible luminescent thermometers.

Encouraged by the low in vitro toxicity and high brightness of our NPs, we moved to in vivo experiments. We administered 150 µL of a 1.0 mg mL^{-1} dispersion of either AISe NCs or commercial Ag_2S NPs in PBS 1x to two female CD1 mice via retro-orbital injection and monitored the evolution of the NIR signal over the course of 3 h under 808 nm excitation (**Figure 3**A). From the comparison of the NIR-II images obtained at different timepoints, it is apparent how the higher brightness of AISe NCs translates to an improvement in image contrast and resolution. When using AISe NCs, the vasculature of the animal became visible and remained distinguishable throughout the whole timespan of the measurement (albeit with a partial loss of overall intensity and, consequently, resolution, Figure S7, Supporting Information), suggesting a long permanence time of our AISe NCs in the vascular system. To that end, it should be noted that we also obtained high-resolution images of the vessels of a mouse's hindlimb in a separate set of experiments, wherein the vasculature of the animal is clearly distinguishable (Figure S8, Supporting Information). Note that under identical experimental conditions (including exposure time) imaging of the vasculature was not possible using commercial Ag_2S NPs. Moreover, the time course of the fluorescence signal generated by AISe NCs and Ag_2S NPs is completely different. This becomes evident when observing the trend of the fluorescence intensity generated at the liver and at the femoral vessels (Figure 3B). For Ag_2S NPs, the NIR intensity decreased at both locations to 40–45% of the maximum value over the course of 3 h. On the other hand, the signal coming from AISe NCs at the liver increased over time, and the intensity of the emission at the femoral vessels only decreased by 15% 3 h after injection. This prolonged imaging of the vasculature via FI is not common and it was ascribed to the unique combination of bright emission and surface modification of the nanostructures. First, the encapsulation in PEGylated phospholipids is expected to minimize the formation of a protein corona around the AISe NCs.[44,45] In addition, the surface modification with maleimide was shown to induce a strong interaction with cell membranes via surface thiols.[46] Therefore, specific interaction with cellular components of the blood vessels (mainly epithelial cells) could be expected, which contribute to extended permanence time within the vascular system.[47] Note that in an additional long-term experiment (Figure S9, Supporting Information) no signal arising from AISe NCs could be observed in correspondence of the blood vessels 24 h after injection of the contrast agents. This observation suggests that the AISe NCs, although residing in the vasculature for an extended period, do not mark permanently the vessels, thus curbing worries regarding long-term effects related to accumulation.

Motivated by the apparent advantage of using AISe NCs in vasculature imaging, we applied principal components analysis (PCA) to the set of in vivo images obtained in the time

© 2021 The Authors. Small published by Wiley-VCH GmbH

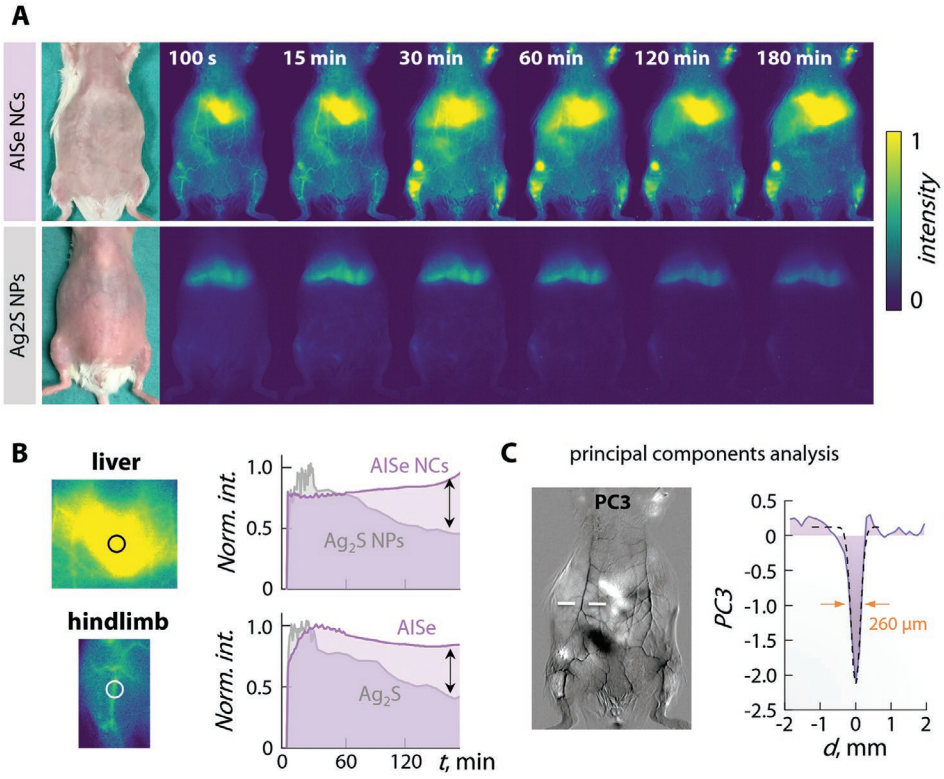

Figure 3. A) Comparison of the performance of AISe NCs and commercial Ag_2S NPs as contrast agents: Picture of the CD1 female mouse before injection and time-course NIR images taken under 808 nm excitation at different time points after retro-orbital injection of 150 µL of a 1.0 mg mL^{-1} dispersion of either AISe NCs (top) or Ag_2S NPs (bottom) in PBS 1x. B) Comparison of the temporal evolution of the NIR signal at the liver (top) and at the femoral vessels (bottom) of two mice injected with AISe NCs (purple) and Ag_2S NPs (gray), respectively. The corresponding areas for the mouse injected with AISe NCs are also indicated. C) Third component (PC3) of the PCA and intensity profile measured in correspondence of the gap between the white segments. Note how the signal passes from positive to negative values from the surrounding tissues to the vessel. The thickness of the vessel (in orange) was obtained as the full width at half maximum of the Gaussian fit (dashed black line) to the data.

frame of the experiment.[48] Our goal was to check if a clearer distinction between the veins/arteries and the surrounding tissues could be achieved. The rationale for using PCA is that this analysis converts a set of observations based on certain variables into another set of linearly uncorrelated new variables ordered according to their importance.[49,50] Hence the pixels containing static or slowly variable signals (highly correlated across the time frames) could be separated from the ones with faster dynamics (a detailed description of the procedures applied to our set of data is described in the Supporting Information).[51] Therefore, in some components (PC*X*, with $X \geq 1$), certain organs could be better distinguished than others. Since the accumulation of the NCs was preferential at the liver, it comes as no surprise that this organ would be in the spotlight in the first components (Figure S10, Supporting Information).[12] For our purposes, however, PC3 is particularly interesting. We selected the right epigastric *cranialis* artery and vein as representative vessels in the right abdominal region (in correspondence of the white segments in Figure 3C, left) and analyzed the projection of the pixels corresponding to the vessel onto PC3 (Figure 3C, right). The thickness of the vessel can be retrieved from a Gaussian fit of the signal and considering the full width at half maximum of the fitting curve (260 µm in this case). What is even more interesting is that, aside from a difference in the magnitude, in PC3 a change in the sign of the signal arising from the vessel and the surrounding tissue can also be observed. This means that, for at least one of the new linearly independent variables, the behavior presented by the vessels was in direct opposition to the one of the surrounding tissues. For this reason, the vessels became markedly visible in this component of the PCA (Figure 3C). Moreover, although PC1 and PC2 did not highlight the vasculature as well as PC3, the contrast offered by them was still remarkable (Figure S10, Supporting Information). Overall, the analysis suggests a good capability of the AISe NCs to work as a contrast agent in enhanced angiography. The extended permanence time of AISe NCs in the vasculature make them suited for applications in angiography and detection of local deficiencies in blood perfusion caused by, for example, stroke.[15,52,53]

Additional confirmation of the capability of the developed AISe NCs to act as effective vasculature markers was obtained from ex vivo NIR images (**Figure 4**). Strong NIR signal was observed in correspondence of blood vessels in the organs. As it can be observed, the vasculature is highlighted in a wide number of organs, such as dorsal skin and muscle, the kidneys, and even the brain. Regarding the two latter organs, the internal vasculature of the kidneys is well resolved in their sagittal and transversals sections, while the characteristic Polygon

© 2021 The Authors. Small published by Wiley-VCH GmbH

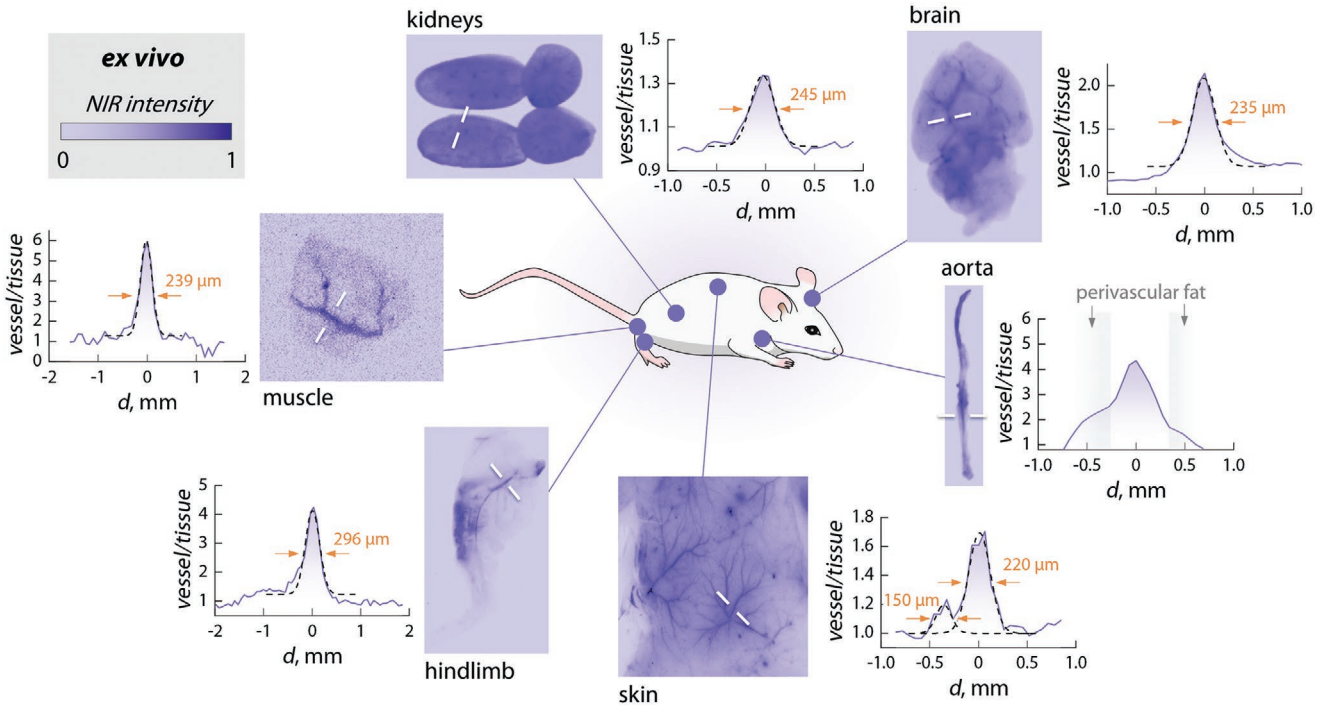

Figure 4. Ex vivo NIR images of selected tissues along with the ratio between the signal arising from the vessel and the surrounding tissue calculated along the direction identified by the white segments. The diameter of the vessels, obtained as the full width at half maximum of a Gaussian fit (dashed black lines), is indicated in orange. In the case of the aorta, this analysis is challenging; therefore, the areas occupied by the perivascular fat are shaded in gray and the ratio is calculated versus the background of the image.

of Willis is observed prior to any dissection in the ventral part of the brain. To further confirm this preferential accumulation in the vasculature, we dissected the aorta: a stronger signal was observed at the vessel compared to the superficial perivascular fat, similarly to what was seen ex vivo for the femoral vessels in the right hindlimb. Depending on the analyzed part of the animal, the contrast achieved with AISe NCs varies, with some vessels (e.g., those in the muscle of the hindlimb and in the skin) being better discerned than others (e.g., those in the kidneys). As concluded from the profiles obtained along selected regions, the ratio between the signal coming from the vessel and the surrounding tissue was in the 1.3–6 range. These values are large enough to allow for a clear differentiation of the vessels and to retrieve their diameter from a Gaussian fit of the profiles. For the selected vessels, diameters ranging from 150 to 300 µm were found, similarly to the size observed in other works for major blood vessels in mice.[25,54]

Lastly, to further confirm the amenability of the developed AISe NCs for in vivo applications, we conducted a toxicologic screening of mice that received a single injection of AISe NCs. The injected dose was analogous to the one used for fluorescence imaging experiments (150 µL, 1 mg mL^{-1}). We then selected a set of biomarkers whose variations can unveil potential pathological processes. Because nanoparticles biodistribution is mainly dictated by the reticuloendothelial system, we considered hepatotoxicity as one of the main potential side-effects.[55] Toxic effects to other organs were also considered, such as hyperlipidemia and bone toxicity. A detailed list of these 12 markers is reported in the Experimental Section. Notably, the concentration of all selected biomarkers remained unaltered when comparing mice injected with AISe NCs and a control group injected with vehicle sterile saline solution (0.9% NaCl; Figure S11, Supporting Information). None of these biomarkers shows statistically relevant differences among groups. These data evidence that at the tested conditions, AISe NCs administered intravenously are not toxic for the main homeostatic systems in CD1 mice. Along with no appreciable difference in weight trend (Figure S12, Supporting Information), these experiments indicate that the developed contrast agents do not display toxicity at one-week time point.

3. Conclusion

We have herein presented the first example of $AgInSe_2$-based contrast agent for fluorescence imaging in the second biological window (NIR-II). The emission of these nanoparticles is shifted toward longer wavelengths compared to the usual emission featured by $AgInSe_2$ due to an uncommon crystal structure, imparted by the used Ag_2S-seed mediated synthesis. Upon transfer to water with the aid of maleimide-bearing phospholipids, nanocapsules composed of several $AgInSe_2$ nanoparticles are formed, which feature high colloidal stability and lack of in vitro cytotoxicity. Their brighter emission and longer permanence time within the vascular system compared to commercial Ag_2S nanoparticles make these nanocapsules an invaluable addition to the currently relatively limited library of contrast agents for near infrared fluorescence imaging. We also showed that the use of PCA allows observing more clearly the vasculature upon dynamical acquisition of fluorescence images

© 2021 The Authors. Small published by Wiley-VCH GmbH

after injection of $AgInSe_2$ nanocapsules. Importantly, no toxicity was induced in mice injected with these nanocapsules over the course of one week, as confirmed by the screening of several relevant biomarkers and the monitoring of weight gain.

Since the improvement of the performance of fluorescence imaging passes through the development of brighter contrast agents, this study represents an important step in this direction. While the developed $AgInSe_2$-based nanocapsules already perform better than commercially available Ag_2S nanoparticles, there is plenty of room for improvement via adjustment of the reaction conditions and exploitation of selective cation exchange procedures. Future research effort will therefore be directed along these lines.

4. Experimental Section

Chemicals: Silver(I) oxide (Ag_2O, 99.9% metal basis, Alfa Aesar), indium(III) acetate ($In(OAc)_3$, 99.99% metal basis, Alfa Aesar), DDT (≥98%, Sigma-Aldrich), 1-octadecene (ODE, 90%, tech), oleylamine (OLA, 80–90%, Fisher), selenium powder (Se, powder, −100 mesh, ≥99.5% trace metals basis, Fisher), tributyl phosphine (TBP, 95%, Fisher), TCE (99%, extra pure), acetone (≥99%, Fisher), 1,2-distearoyl-*sn*-glycero-3-phosphoethanolamine-*N*-[maleimide(polyethylene glycol)-2000] (ammonium salt) Maleimide (DSPE-PEG2000-MAL), Avanti Polaris), acetone (≥99%, Fisher). All chemicals were used as received. Commercial PEGylated Ag_2S NPs in PBS were obtained from Shizou NIR/optics Technology Co. Ltd (Suzhou, China)

Synthesis of AISe NPs: The synthesis of AISe NPs was performed according to a previously reported procedure.[34] A Se precursor solution was initially prepared dissolving 0.4 mmol (31.6 mg) of Se in 0.1 mL of TBP and 0.3 mL of ODE. In the meantime, 0.05 mmol (6.2 mg) of AgO and 0.05 mmol (14.6 mg) of $In(OAc)_3$ were added to a mixture of 0.25 mL of DDT and 5 mL of ODE. The mixture was degassed under vacuum for 30 min at 90 °C, followed by addition of 0.25 mL of OLA. The mixture was degassed for further 30 min under vacuum, backfilled with Ar, stirred until it became clear and the temperature was then set to 190 °C. Upon reaching the target temperature, 0.2 mL of Se precursor was swiftly injected and the solution was maintained at 190 °C for 90 min. The product was precipitated by adding acetone, followed by centrifugation at 3820 rcf for 30 min. The supernatant was discarded and the pellet redispersed in 3 mL of TCE. The sample was stored at −20 °C for further use.

Transfer of $AgInSe_2$ NPs to Aqueous Media: Typically, 0.2 mL of AISe NPs in TCE (0.5 mg mL^{-1}) were transferred in a 1.5 mL centrifuge tube and precipitated with 1 mL of methanol. The NPs were collected via centrifugation at 11093 rcf for 2 min. The precipitate was redispersed in 0.5 mL of chloroform and sonicated for 3 min. Meanwhile, 20.0 mg of DSPE-PEG_{2000}-MAL was dissolved in 1.5 mL of chloroform in a 50 mL round-bottom flask and sonicated for 3 min. The dispersion of $AgInSe_2$ in chloroform was added to the solution of DSPE-PEG_{2000}-MAL and sonicated for 2 min at room temperature. The chloroform was slowly evaporated at room temperature with the aid of a rotary evaporator to form a thin film on the wall of the flask. The rehydration of the film was performed adding 3 mL of water followed by sonicating for 3 min, which yielded the final AISe nanocapsules AISe nanocapsules. The nanocapsules were precipitated twice via centrifugation at 11093 rcf for 10 min at 10 °C, redispersed in water (or PBS 1x), stored at 4 °C, and used within 3 days from their preparation.

Characterization: The morphology and size of the NPs and NCs was investigated using a JEM1400 Flash (JEOL) TEM microscope). Elemental mapping was performed on a JEOL JSM 7600F scanning electron microscope. The optical extinction spectra were recorded at room temperature with a UV–vis–NIR spectrophotometer (Perkin Elmer Lambda1050) using a 1 nm step in the 400–2000 nm range. Infrared spectra were obtained in transmission mode on a Spectrum Two instrument (Perkin Elmer) in the 450–4000 cm^{-1} range with 4 cm^{-1} resolution, preparing KBr tablets containing 1 wt% of the analyzed material. Lifetime measurements were performed by using an Optical Parametric Oscillator (Quanta Ray) pumped by a frequency tripled neodymium-doped yttrium aluminum garnet (Nd:YAG) laser operating at 355 nm. The Optical Parametric Oscillator operates at 800 nm and provides 10 ns pulses with an average energy of 0.2 J and with a repetition rate of 10 Hz. For temperature-dependent studies, a cuvette containing the AISe NCs dispersion was placed in a qpod 2e (Quantum Northwest, Inc.), using an 850 nm long-pass filter (Thorlabs FEL850) in the emission path. The emitted radiation was spectrally sorted by a high-brightness monochromator (Shamrock 163, Andor) and detected with an infrared photomultiplier (Hamamatsu H1033C). To record the photoluminescence decay curves, the photomultiplier was connected to a digital oscilloscope (Le Croy Wave Runner 500). The absolute PLQY was measured with a 6 in. diameter integrating sphere (Labsphere, 4P-GPS-060-SF). The sample cuvette (5 mm path length) was mounted at the center of the sphere. Light from a pigtailed 808 nm laser (Omicrom, BrixX808-2500-HP-FC) was collimated onto the sample with a beam diameter of 2.5 mm. The collected signal was sent to a monochromator (Horiba, iHR320) for wavelength selection and detected with an NIR InGaAs photodetector (Horiba, DSS-IGA020TC). Powder X-ray diffraction (PXRD) measurement was performed on a Rigaku D/max-γB diffractometer working in the Bragg-Brentano geometry (θ–2θ) with a step of 0.03° in the 20–60° range. The hydrodynamic diameter and Z-potential were measured at different temperatures with a Zetasizer Ultra (Malvern Panalytical, Ltd.) using a 1 cm cuvette containing dispersions in TCE, water, or PBS.

In Vitro Cytotoxicity Tests: Human cervical adenocarcinoma cells (HeLa cell line, ATCC, UK) were grown in Dulbecco's modified Eagle's medium (Hyclone, GE Healthcare, USA) supplemented with fetal calf serum (10%, Gibco) and 0.5% of antibiotics (penicillin G [10000 U mL^{-1}] and streptomycin sulfate [10 000 mg mL^{-1}] (Gibco)). Cells were grown in a Thermo Scientific Midi 40 CO_2 Incubator (Thermo Fisher Scientific Inc.) with a 5% CO_2 atmosphere, a 95% relative humidity and a constant temperature of 37 °C.

The viability of HeLa cells exposed to AISe NCs was analyzed by the 3-(4,5-dimethylthiazol-2-yl)-2,5-diphenyltetrazolium bromide (MTT) assay.[56] Twenty-four hours after appropriate treatments with AISe NCs, MTT solution was added to each well at a concentration of 0.5 ng mL^{-1} and plates were incubated at 37 °C for 2 h. The resulting formazan crystals were dissolved by the addition of dimethylsulfoxide and absorbance was measured at 542 nm. Cell viability was estimated as a percentage relative to the mean absorption obtained from control cells (not incubated with the AISe NCs; 100% viability).

Plasma Extraction and Toxicological Screening: Animals were sacrificed one week after retro-orbital injection of 150 µL of a 1 mg mL^{-1} AISe NCs dispersion via beheading under deep isoflurane anesthesia. Blood was immediately collected in tubes containing heparin at a final concentration of 50 U for 1 mL of blood. The tubes were gently inverted six times and immediately centrifuged at 4 °C for 20 min at a centrifugation speed of 3000 *g*. The supernatants were collected and stored at −80 °C until their biochemical determination. The monitored biomarkers are aspartate and alanine aminotransferase (AST/GOT and ALT/GPT), alkaline phosphatase, creatinine (Cre), albumin (Alb), total and direct bilirubin (BT and BD), hemoglobin (Hb), total triglycerides, total cholesterol, and cholesterol bounded high and low lipodensity proteins. Biochemical commercial kits from SPINREACT were used to perform colorimetric assays which are based on absorbance changes to obtain chemical determination. Statistical analysis was performed using the GraphPad 8.0 software and Mann–Whitney and multiple way analysis of variance tests were conducted for toxicologic and weight data analysis, respectively.

Imaging System: NIR-II in vivo and ex vivo images were obtained with an InGaAs NIR camera (ZephIRTM 1.7). A fiber-coupled diode laser operating at 808 nm was used as excitation source (LIMO30-F200-DL808). The illumination power density was controlled by adjusting the diode current and set to 50 mW cm^{-2} (a low power density that prevented excessive tissue heating and subsequent drying) and the laser height was adjusted to illuminate the whole animal. A short-pass filter (Thorlabs FES 850) was placed immediately in front of the laser

© 2021 The Authors. Small published by Wiley-VCH GmbH

fiber to minimize specular and diffuse reflection effects. Additionally, 3 long-pass filters (Thorlabs FEL850) were used to minimize tissue autofluorescence signal.

Animal Handling: In vivo experiments were approved by the regional authority for animal experimentation of the Comunidad de Madrid and were conducted in agreement with the Universidad Autónoma de Madrid (UAM) Ethics Committee, in compliance with the European Union directives 63/2010UE and Spanish regulation RD 53/2013. For this study, CD1 female mice (24 weeks old, weighing ≈45 g) bred at the animal facility of UAM were used. Each mouse was first shaven completely with depilatory cream to minimize autofluorescence derived from hair. Then, the animal was anesthetized prior to the imaging experiments in an induction chamber with a continuous flow of 3% isoflurane (Forane, AbbVie Spain, S.L.U.) and 2 L min^{-1} of 100% O_2 until loss of righting reflex was confirmed and breathing rhythm was significantly slowed down. Anesthesia was maintained throughout the experiments by means of facemask inhalation of 1.5% isoflurane and 0.5 L min^{-1} of O_2. Throughout the experiment, the core body temperature was monitored with a rectal probe and kept at 36±1 °C using a heating pad.

In Vivo Fluorescence Imaging: With the animal deeply anesthetized, 150 µL of a 1 mg mL^{-1} dispersion of AISe NCs was administrated in PBS 1x via retro-orbital injection. Six videos of 5 min each, with a nonirradiation period of 1 min in between to minimize laser-induced animal heating, were obtained for the first 36 min. A second set of photos were obtained acquiring one photo every 10 min for the next 150 min. To perform principal component analysis (PCA), the image frames obtained in the first 10 min after injection of AISe Ncs were loaded into an array using MATLAB software and the princomp function was used. For acquiring high-resolution images of the hind limb, 150 µL of a 1 mg mL^{-1} dispersion of AISe NCs in PBS 1x were injected in the tail of the mouse.

Ex Vivo Fluorescence Imaging: After 3 h of in vivo imaging, the animal was immediately euthanized by beheading after induction of deep anesthesia with isoflurane under a constant oxygen flow rate of 2 mL min^{-1} and a concentration of 4% of isoflurane. The organs were removed and washed thoroughly with 0.9% NaCl solution at room temperature. The time between sacrifice and imaging was shorter than 5 min.

Supporting Information

Supporting Information is available from the Wiley Online Library or from the author.

Acknowledgements

J.Y. acknowledges the support from the China Scholarship Council (CSC File No. 201704910867). R.M. acknowledges the support of the European Commission through the European Union's Horizon 2020 research and innovation program under the Marie Skłodowska-Curie Grant Agreement No. 797945 (LANTERNS). P.R. is grateful for a Juan de la Cierva – Incorporación scholarship (IJC2019-041915-I). This work was supported by the Ministerio de Ciencia e Innovación de España under projects MAT2016-75362-C3-1-R, MAT2017-83111R, and MAT2017-85617-R, by the Instituto de Salud Carlos III (PI16/00812), by the Comunidad Autónoma de Madrid (B2017/BMD3867RENIMCM, PID2019-106211RB-I00), and cofinanced by the European Structural and investment fund. Additional funding was provided by the European Union Horizon 2020 FETOpen project NanoTBTech (801305), the Fundación para la Investigación Biomédica del Hospital Universitario Ramón y Cajal project IMP18_38 (2018/0265), and also by COST action CA17140. E.X. is grateful for a Juan de la Cierva Formación scholarship (FJC2018-036734-I). The authors thanks Prof. Jorge Rubio-Retama for elemental mapping measurements.

Conflict of Interest

The authors declare no conflict of interest.

Data Availability Statement

The data that support the findings of this study are available from the corresponding author upon reasonable request.

Keywords

bioimaging, in vivo, infrared, selenides, semiconductor nanoparticles

Received: June 16, 2021
Published online:

[1] E. Ximendes, A. Benayas, D. Jaque, R. Marin, *ACS Nano* **2021**, *15*, 1917.
[2] S. L. Jacques, *Phys. Med. Biol.* **2013**, *58*, R37.
[3] A. Bashkatov, E. Genina, V. Kochubey, V. Tuchin, *J. Phys. D: Appl. Phys.* **2005**, *38*, 2543.
[4] P. Reineck, B. C. Gibson, *Adv. Opt. Mater.* **2017**, *5*, 1600446.
[5] G. Hong, A. L. Antaris, H. Dai, *Nat. Biomed. Eng.* **2017**, *1*, 0010.
[6] A. M. Smith, M. C. Mancini, S. Nie, *Nat. Nanotechnol.* **2009**, *4*, 710.
[7] E. Hemmer, A. Benayas, F. Legare, F. Vetrone, *Nanoscale Horiz.* **2016**, *1*, 168.
[8] E. Hemmer, N. Venkatachalam, H. Hyodo, A. Hattori, Y. Ebina, H. Kishimoto, K. Soga, *Nanoscale* **2013**, *5*, 11339.
[9] G. Hong, J. C. Lee, A. Jha, S. Diao, K. H. Nakayama, L. Hou, T. C. Doyle, J. T. Robinson, A. L. Antaris, H. Dai, J. P. Cooke, N. F. Huang, *Circ. Cardiovasc. Imaging* **2014**, *7*, 517.
[10] J. Hu, D. H. Ortgies, E. Martín Rodríguez, F. Rivero, R. Aguilar Torres, F. Alfonso, N. Fernández, G. Carreño-Tarragona, L. Monge, F. Sanz-Rodriguez, M. d. C. Iglesias, M. Granado, A. L. García-Villalon, J. García Solé, D. Jaque, *Adv. Opt. Mater.* **2018**, *6*, 1800626.
[11] J. Hu, D. H. Ortgies, R. Aguliar Torres, N. Fernández, L. Porto, E. Martín Rodríguez, J. García Solé, D. Jaque, F. Alfonso, F. Rivero, *Adv. Funct. Mater.* **2017**, *27*, 1703276.
[12] K. Welsher, S. P. Sherlock, H. Dai, *Proc. Natl. Acad. Sci. U. S. A.* **2011**, *108*, 8943.
[13] D. J. Naczynski, M. C. Tan, M. Zevon, B. Wall, J. Kohl, A. Kulesa, S. Chen, C. M. Roth, R. E. Riman, P. V. Moghe, *Nat. Commun.* **2013**, *4*, 2199.
[14] Y. Zhang, G. Hong, Y. Zhang, G. Chen, F. Li, H. Dai, Q. Wang, *ACS Nano* **2012**, *6*, 3695.
[15] G. Hong, S. Diao, J. Chang, A. L. Antaris, C. Chen, B. Zhang, S. Zhao, D. N. Atochin, P. L. Huang, K. I. Andreasson, C. J. Kuo, H. Dai, *Nat. Photonics* **2014**, *8*, 723.
[16] D. Jaque, C. Richard, B. Viana, K. Soga, X. Liu, J. G. Solé, *Adv. Opt. Photonics* **2016**, *8*, 1.
[17] Y. Shen, H. D. A. Santos, E. C. Ximendes, J. Lifante, A. Sanz-Portilla, L. Monge, N. Fernández, I. Chaves-Coira, C. Jacinto, C. D. S. Brites, L. D. Carlos, A. Benayas, M. C. Iglesias-de la Cruz, D. Jaque, *Adv. Funct. Mater.* **2020**, *30*, 2002730.
[18] D. Ruiz, B. del Rosal, M. Acebrón, C. Palencia, C. Sun, J. Cabanilla-González, M. López-Haro, A. B. Hungría, D. Jaque, B. H. Juarez, *Adv. Funct. Mater.* **2017**, *27*, 1604629.
[19] D. Yan, Y. He, Y. Ge, G. Song, *Sens. Actuators, B* **2017**, *240*, 863.

© 2021 The Authors. Small published by Wiley-VCH GmbH

[20] B. del Rosal, D. Ruiz, I. Chaves-Coira, B. H. Juárez, L. Monge, G. Hong, N. Fernández, D. Jaque, *Adv. Funct. Mater.* **2018**, *28*, 1806088.
[21] H. D. A. Santos, E. C. Ximendes, M. d. C. Iglesias-de la Cruz, I. Chaves-Coira, B. del Rosal, C. Jacinto, L. Monge, I. Rubia-Rodríguez, D. Ortega, S. Mateos, J. GarcíaSolé, D. Jaque, N. Fernández, *Adv. Funct. Mater.* **2018**, *28*, 1803924.
[22] C. Li, Y. Zhang, M. Wang, Y. Zhang, G. Chen, L. Li, D. Wu, Q. Wang, *Biomaterials* **2014**, *35*, 393.
[23] D. H. Ortgies, Á. L. García-Villalón, M. Granado, S. Amor, E. M. Rodríguez, H. D. A. Santos, J. Yao, J. Rubio-Retama, D. Jaque, *Nano Res.* **2019**, *12*, 749.
[24] Y. Zhang, Y. Zhang, G. Hong, W. He, K. Zhou, K. Yang, F. Li, G. Chen, Z. Liu, H. Dai, Q. Wang, *Biomaterials* **2013**, *34*, 3639.
[25] H. D. A. Santos, I. Zabala Gutiérrez, Y. Shen, J. Lifante, E. Ximendes, M. Laurenti, D. Méndez-González, S. Melle, O. G. Calderón, E. López Cabarcos, N. Fernández, I. Chaves-Coira, D. Lucena-Agell, L. Monge, M. D. Mackenzie, J. Marqués-Hueso, C. M. S. Jones, C. Jacinto, B. del Rosal, A. K. Kar, J. Rubio-Retama, D. Jaque, *Nat. Commun.* **2020**, *11*, 2933.
[26] D. Ruiz, M. Mizrahi, H. D. A. Santos, D. Jaque, C. M. S. Jones, J. Marqués-Hueso, C. Jacinto, F. G. Requejo, A. Torres-Pardo, J. M. González-Calbet, B. H. Juárez, *Nanoscale* **2019**, *11*, 9194.
[27] L. M. Maestro, P. Haro-González, B. del Rosal, J. Ramiro, A. Caamano, E. Carrasco, A. Juarranz, F. Sanz-Rodríguez, J. G. Solé, D. Jaque, *Nanoscale* **2013**, *5*, 7882.
[28] A. Ortega-Rodriguez, Y. Shen, I. Zabala Gutierrez, H. D. A. Santos, V. Torres Vera, E. Ximendes, G. Villaverde, J. Lifante, C. Gerke, N. Fernandez, O. G. Calderon, S. Melle, J. Marques-Hueso, D. Mendez-Gonzalez, M. Laurenti, C. M. S. Jones, J. M. Lopez-Romero, R. Contreras-Caceres, D. Jaque, J. Rubio-Retama, *ACS Appl. Mater. Interfaces* **2020**, *12*, 12500.
[29] Y. Shen, J. Lifante, E. Ximendes, H. D. A. Santos, D. Ruiz, B. H. Juarez, I. Zabala Gutierrez, V. Torres Vera, J. Rubio Retama, E. Martin Rodriguez, D. H. Ortgies, D. Jaque, A. Benayas, B. del Rosal, *Nanoscale* **2019**, *11*, 19251.
[30] J.-Y. Chang, G.-Q. Wang, C.-Y. Cheng, W.-X. Lin, J.-C. Hsu, *J. Mater. Chem.* **2012**, *22*, 10609.
[31] X. Hu, T. Chen, Y. Xu, M. Wang, W. Jiang, W. Jiang, *J. Lumin.* **2018**, *200*, 189.
[32] S. E. Creutz, R. Fainblat, Y. Kim, M. C. De Siena, D. R. Gamelin, *J. Am. Chem. Soc.* **2017**, *139*, 11814.
[33] D. Deng, L. Qu, Y. Gu, *J. Mater. Chem. C* **2014**, *2*, 7077.
[34] M. A. Langevin, A. M. Ritcey, C. N. Allen, *ACS Nano* **2014**, *8*, 3476.
[35] M. T. Ng, C. B. Boothroyd, J. J. Vittal, *J. Am. Chem. Soc.* **2006**, *128*, 7118.
[36] B. A. Tappan, M. K. Horton, R. L. Brutchey, *Chem. Mater.* **2020**, *32*, 2935.
[37] T. Bai, S. Xing, C. Li, Z. Shi, S. Feng, *Chem. Commun. (Cambridge, U. K.)* **2016**, *52*, 8581.
[38] J. M. J. M. Ravasco, H. Faustino, A. Trindade, P. M. P. Gois, *Chem. - Eur. J.* **2019**, *25*, 43.
[39] T. Li, S. Takeoka, *Int. J. Nanomed.* **2014**, *9*, 2849.
[40] O. S. Oluwafemi, B. M. M. May, S. Parani, N. Tsolekile, *Mater. Sci. Eng., C* **2020**, *106*, 110181.
[41] S. K. Panigrahi, A. K. Mishra, *J. Photochem. Photobiol., C* **2019**, *41*, 100318.
[42] F. Wang, J. Wang, X. Liu, *Angew. Chem., Int. Ed. Engl.* **2010**, *49*, 7456.
[43] H. Santos, D. Ruiz, G. Lifante, C. Jacinto, B. Juarez, D. Jaque, *Nanoscale* **2017**, *9*, 2505.
[44] T. Lima, K. Bernfur, M. Vilanova, T. Cedervall, *Sci. Rep.* **2020**, *10*, 1129.
[45] P. d. Pino, B. Pelaz, Q. Zhang, P. Maffre, G. U. Nienhaus, W. J. Parak, *Mater. Horiz.* **2014**, *1*, 301.
[46] A. G. Torres, M. J. Gait, *Trends Biotechnol.* **2012**, *30*, 185.
[47] R. B. Huang, S. Mocherla, M. J. Heslinga, P. Charoenphol, O. Eniola-Adefeso, *Mol. Membr. Biol.* **2010**, *27*, 190.
[48] E. M. C. Hillman, A. Moore, *Nat. Photonics* **2007**, *1*, 526.
[49] S. Wold, K. Esbensen, P. Geladi, *Chemom. Intell. Lab. Syst.* **1987**, *2*, 37.
[50] R. Vidal, Y. Ma, S. S. Sastry, in *Generalized Principal Component Analysis*, Springer, New York, NY **2016**, Ch. 2, p. 25, https://doi.org/10.1007/978-0-387-87811-9_2.
[51] N. Le, S. Song, Q. Zhang, R. K. Wang, *Quant. Imaging Med. Surg.* **2017**, *7*, 654.
[52] R. Bhavane, Z. Starosolski, I. Stupin, K. B. Ghaghada, A. Annapragada, *Sci. Rep.* **2018**, *8*, 14455.
[53] F. C. Piccolino, L. Borgia, E. Zinicola, M. Iester, S. Torrielli, *Ophthalmology* **1996**, *103*, 1837.
[54] G. Hong, J. C. Lee, J. T. Robinson, U. Raaz, L. Xie, N. F. Huang, J. P. Cooke, H. Dai, *Nat. Med.* **2012**, *18*, 1841.
[55] Y. Tang, X. Wang, J. Li, Y. Nie, G. Liao, Y. Yu, C. Li, *ACS Nano* **2019**, *13*, 13015.
[56] T. L. Riss, R. A. Moravec, A. L. Niles, S. Duellman, H. A. Benink, T. J. Worzella, L. Minor, in *Assay Guidance Manual* (Eds: G. S. Sittampalam, A. Grossman, K. Brimacombe, M. Arkin, D. Auld, C. Austin, J. Baell, B. Bejcek, J. M. M. Caaveiro, T. D. Y. Chung, N. P. Coussens, J. L. Dahlin, V. Devanaryan, T. L. Foley, M. Glicksman, M. D. Hall, J. V. Haas, S. R. J. Hoare, J. Inglese, P. W. Iversen, S. D. Kahl, S. C. Kales, S. Kirshner, M. Lal-Nag, Z. Li, J. McGee, O. McManus, T. Riss, O. J. Trask Jr., J. R. Weidner, M. J. Wildey, M. Xia, X. Xu), Eli Lilly and Company and the National Center for Advancing Translational Sciences, Bethesda, MD **2004**.

© 2021 The Authors. Small published by Wiley-VCH GmbH